INSTITUTE OF PHYSICS PUBLISHING JOURNAL OF PHYSICS D: APPLIED PHYSICS
J. Phys. D: Appl. Phys. **39** (2006) 3717–3725 doi:10.1088/0022-3727/39/17/001

Magnetic and optical properties of (GaMn)N nanocrystalline powders prepared by the aerosol-assisted vapour phase synthesis and anaerobic imide route methods

J B Gosk[1,2], M Drygaś[3], J F Janik[3], M Palczewska[4], R T Paine[5] and A Twardowski[1]

[1] Institute of Experimental Physics, Warsaw University, Hoża 69, 00-681 Warsaw, Poland
[2] Faculty of Physics, Warsaw University of Technology, Koszykowa 75, 00-662 Warsaw, Poland
[3] Faculty of Fuels and Energy, AGH University of Science and Technology, Al. Mickiewicza 30, 30-059 Kraków, Poland
[4] Institute of Electronic Materials Technology, Wólczyńska 133, 01-919 Warsaw, Poland
[5] Department of Chemistry, University of New Mexico, Albuquerque, NM 87131, USA

Received 21 April 2006, in final form 21 July 2006
Published 17 August 2006
Online at stacks.iop.org/JPhysD/39/3717

Abstract
Herein, we report a study on magnetic and optical properties of hexagonal (GaMn)N nanocrystalline powders obtained by two methods: aerosol-assisted vapour phase synthesis and anaerobic imide route. Measurements of the magnetization as a function of temperature and magnetic field for the powders show a typical paramagnetic behaviour. In addition, antiferromagnetic contribution originating from a residual MnO by-product and a small ferromagnetic contribution are observed. Magnetization measured as the function of magnetic field shows a smaller saturation effect than expected for non-interacting Mn-ions. Electron paramagnetic resonance (EPR) measurements reveal a single, structureless resonance line with a g-factor equal to 2.008±0.003 indicating a presence of Mn^{2+}-centres in the samples. Both magnetic and EPR measurements suggest weak AF interactions between Mn-ions incorporated in (GaMn)N.

1. Introduction

Spintronics' demands for ferromagnetic (FM) semiconductors with high Curie temperature (T_C) pose a great challenge for physicists and materials scientists. In this regard, the carrier-induced ferromagnetism observed in (GaMn)As and (InMn)As has not met with due expectations [1, 2]. The highest T_C obtained to date reaches about 170 K in (GaMn)As and is still far from room temperature [3]. On the other hand, the theoretical calculations based on the Zener model offer much hope since they predict T_C exceeding room temperature in the system (GaMn)N [4]. However, the feasibility of the assumptions put forward in that work, i.e., the simultaneously large Mn^{+2}-concentrations (d^5 configuration) in the GaN lattice of the order of 5% and hole concentrations of the order of $10^{20}\,cm^{-3}$, can only be confirmed on successfully prepared materials of this kind. The main synthetic problem appears to lie in that the transition metals show very limited solubility in III–V compound semiconductors. Also, it was shown that straightforward extrapolation from (GaMn)As to (GaMn)N crystals is not valid since the itinerant character of the Mn^{2+} +h complex in (GaMn)As is changed to a rather localized Mn^{3+} neutral acceptor state in (GaMn)N [5–7]. Nevertheless, (GaMn)N has been recently the most intensively investigated diluted magnetic semiconductor (DMS) among Group III–V compounds, both experimentally [8–14] and theoretically [15–21].

Many experimental efforts have been undertaken to circumvent the low thermal-equilibrium solid solubility of Mn

in gallium nitride, GaN. So far, several techniques have been employed to prepare (GaMn)N, i.e., ammonothermal technique (AMMONO) [8,9], molecular beam epitaxy (MBE) [6, 22, 23], and metal organic chemical vapour deposition (MOCVD) and subsequent ion implantation/Mn diffusion into GaN templates [13, 14, 24]. Successful preparations of the single crystal and microcrystalline forms of GaN with low and relatively high Mn-contents have also been reported [7, 10]. The magnetic properties of (GaMn)N seem to depend on specific crystal growth conditions. In this regard, (GaMn)N single crystals and microcrystals show paramagnetic (PM) behaviour with antiferromagnetic (AF) d–d interactions [9, 25, 26] while some epitaxial layers reveal a FM response with T_C far above 300 K [12, 14]. However, the origin of the observed ferromagnetism has yet to be clarified. Some authors relate the observation of room temperature ferromagnetism to an intrinsic property of (GaMn)N [12–14] while others link it to the presence of FM Mn–N and/or Ga–Mn precipitates or clusters in the investigated compounds [8–11,26–28]. It should be noted that the reports about ferromagnetism observed in (GaMn)N have been primarily based on magnetization hysteresis loop measurements. However, the magnetization curves alone are not sufficient to draw correct conclusions of this type and could be quite often misleading since, commonly, there is a lack of detailed analysis based on extended magnetization data. Crystallographic characterization alone, also, if precipitates or small clusters are present, is not sufficiently accurate to confirm the origin of intrinsic ferromagnetism of DMS. It is highly misleading to accept arguments that the lack of specific reflections in x-ray diffraction patterns in DMS for possible minor phases (precipitates) mediates against the phases presence since the reflections may be too weak and/or too broad to be observed. The latter is especially true for nanocrystalline powders.

The advantage of magneto-optical spectroscopy, namely measurements of magnetic circular dichroism (MCD), for characterization of DMS magnetic properties has been demonstrated by Ando *et al* [29]. The magnetic field and temperature dependence of the MCD intensity data allowed them to confirm that their $Ga_{1-x}Mn_xN$ film was a PM DMS and that RT ferromagnetism of the sample arose from some unidentified material which was not detected by x-ray diffraction [30]. Dhar and co-workers [22, 31] performed a detailed structural and magnetic characterization of (GaMn)N layers grown on 4H-SiC(0001) by reactive MBE. The TEM study revealed that, for a lower Mn-composition (7.6%), homogeneous (GaMn)N ternary alloys were formed while in the layer with a higher Mn-content (13.7%) Mn-rich clusters embedded in the (GaMn)N alloy matrix were present. Both types of samples exhibited AF Mn–Mn interaction with Curie–Weiss temperature $\Theta = -10.4$ K close to that observed in the case of microcrystalline powders [9]. Additionally, the FM response observed at and above room temperature for the insulating (GaMn)N with the high Mn-content was attributed directly to Mn-clusters in the alloy. It is worth noting that the authors were unable to detect the presence of the clusters by XRD measurements.

Despite these extensive efforts, there is no single model capable of explaining the magnetic properties observed for (GaMn)N and there has yet been no convincing experimental evidence that room temperature T_C is feasible in DMS prepared from gallium nitride. Therefore, there is clearly an urgent need for further research in this field, especially, directed towards new and reproducible methods of (GaMn)N synthesis. In this work, we show that the (GaMn)N nanocrystalline powders with relatively high Mn-concentrations can be successfully prepared by two methods, i.e., aerosol-assisted vapour phase synthesis (AAVS) and anaerobic imide route. In AAVS, in the first stage complex decomposition and partial nitridation reactions take place during the aerosol generation between ammonia and submicrometre-sized droplets containing precursors and solvent (water or methanol). The bulk aerosol powders obtained from this processing are usually subjected to a second-stage pyrolysis under ammonia to complete nitridation of products that have spheroidal particle morphology. The main advantages of the aerosol-assisted process are the utilization of affordable precursors and the fact that all reactions take place within very small liquid and solid particles suspended in a reactive gas stream, which creates more-advantageous conditions for nitridation towards nanosized particles compared with typical one-stage bulk pyrolysis methods. The second utilized synthetic method, i.e., anaerobic imide route, dwells on the application of organometallic precursors and specific reaction conditions (exclusion of air and moisture, relatively low temperatures of synthesis) that result in specific powder characteristics and, in favourable cases, capability to control average crystallite sizes in the nanosized range. Herein, are presented and discussed the magnetization and EPR characterization data for (GaMn)N nanocrystalline powders obtained with these methods.

2. Experimental

In the already published AAVS preparation of (GaMn)N [32], aqueous and methanol-based aerosols of appropriate mixtures of $Ga(NO_3)_3 \cdot xH_2O$ and $Mn(NO_3)_2 \cdot xH_2O$ were reacted in an ammonia rich atmosphere at 1050 °C under specific process conditions to yield raw aerosol powders. This stage was followed by pyrolysis of the powders at 1000 °C, 4 h, under an ammonia flow producing grey-yellowish materials. Three sets of samples differentiated by the initial atomic ratio of Ga/Mn were studied, namely, Ga/Mn equal to approximately 5, 10 and 20. We designate the samples in this order of Ga/Mn ratio as A5, A10, A20 (A—derived from aqueous solutions) and B5, B10, B20 (B—derived from methanol-based solutions), respectively. Additionally, two sets of phase-pure materials, i.e., one derived from the solutions of pure $Ga(NO_3)_3 \cdot xH_2O$ (samples GaN($H_2$0) and GaN(MeOH)) and another made from the solutions of pure $Mn(NO_3)_2 \cdot xH_2O$ (samples MnO(H_2O) and MnO(MeOH)), were used as reference samples. The XRD patterns supplemented with EDX data and oxygen analyses confirmed the hexagonal GaN-type phase and cubic Mn(II)O as the major crystalline phases while suggesting the former as manganese enriched (GaMn)N.

The second method used to make materials in the system GaN/Mn (herein called the imide route) was based on the reported anaerobic preparation of pure nanocrystalline gallium nitride, GaN, from polymeric gallium imide, $\{Ga(NH)_{3/2}\}_n$ [33]. In this route, the insoluble gallium imide precursor is first made from a reaction of diethyl ether-soluble

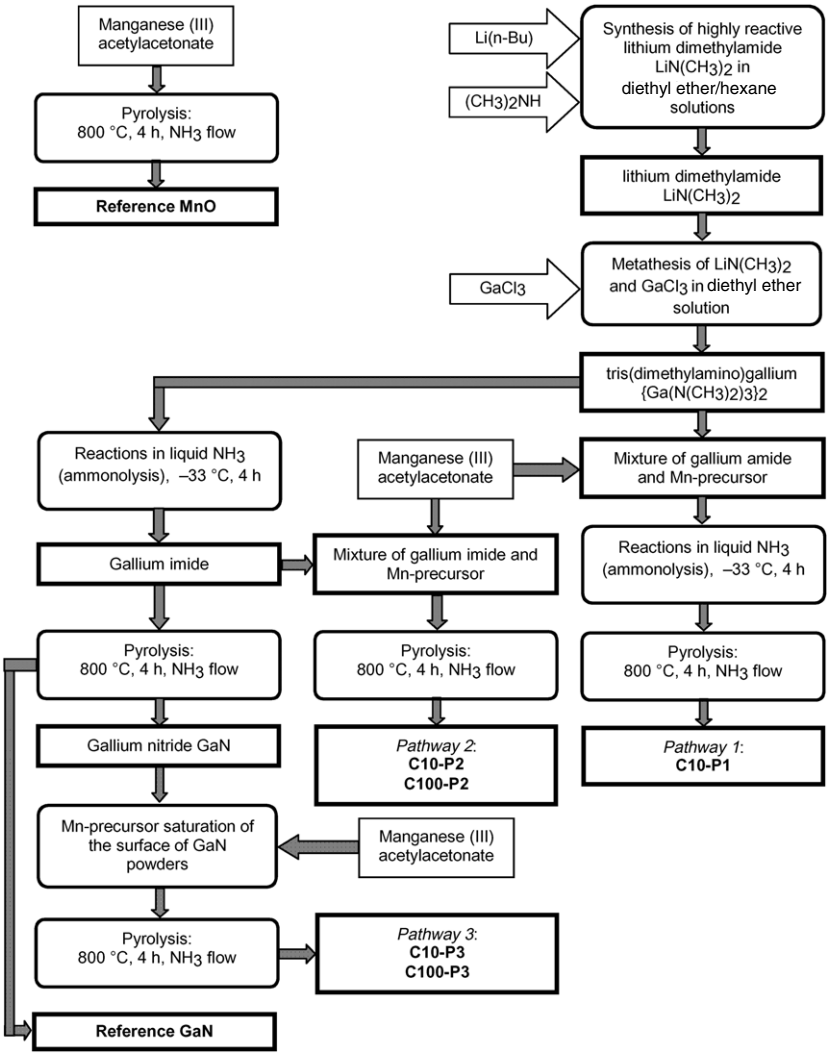

Figure 1. Preparation of various (GaMn)N materials via anaerobic imide route method.

$\{Ga[N(CH_3)_2]_3\}_2$ with liquid ammonia followed by its isolation and pyrolysis at elevated temperatures under a NH_3 flow to result in nano-GaN.

To achieve the synthesis of various Mn-doped materials while conforming to the basic procedure, we employed the addition of a commercially available manganese precursor, i.e., manganese (III) acetylacetonate, at different stages of the imide route scheme as illustrated in figure 1.

Since different chemistry was to play a role in the variant preparation pathways, one expected a range of resulting (GaMn)N materials with, potentially, varying amounts of incorporated manganese. In Pathway 1, an appropriate proportion of the manganese precursor to yield atomic ratio of the metals Ga/Mn = 10/1 was added with stirring to a diethyl ether solution of $\{Ga[N(CH_3)_2]_3\}_2$. Subsequently, the volatiles were removed from the homogeneous solution and the resulting composite powder was subjected to ammonolysis in refluxing liquid ammonia for 4 h. Presumably, this leads to homogeneously dispersed manganese centres in the solid gallium imide. Upon pyrolysis of the precursor at 800 °C, 4 h, under a NH_3 flow, a yellow–brown powder was obtained that was labelled as sample C10-P1. In Pathway 2, appropriate proportions of diethyl ether solutions of the manganese precursor to yield the atomic ratios Ga/Mn = 10/1 and 100/1 were individually mixed with an ether slurry of already made pure gallium imide, $\{Ga(NH)_{3/2}\}_n$. This was followed by removal of volatiles and pyrolyses of the resulting solid precursors under identical conditions as above to afford two related materials, i.e., from system Ga/Mn = 10/1, sample C10-P2 and from system Ga/Mn = 100/1, sample C100-P2. In Pathway 3, appropriate proportions of diethyl ether solutions of the manganese precursor to yield the atomic ratios Ga/Mn = 10/1 and 100/1 were individually mixed with an ether slurry of already prepared at 800 °C pure gallium nitride to achieve a reactive incorporation of Mn on the nitride's surface. Upon removal of volatiles, the resulting solid was pyrolysed as before yielding two materials, i.e., from system Ga/Mn = 10/1, sample C10-P3 and from system Ga/Mn = 100/1, sample C100-P3. The summary of sample labelling including average crystallite sizes of the hexagonal GaN-type phase determined with Scherrer equation from the XRD patterns is shown in table 1.

All products were characterized by powder XRD (Siemens D5000 with Cu K_α source; 2Θ, 20–80°; step size, 0.04).

Table 1. Labelling of samples and, in parentheses, average crystallite sizes of hexagonal GaN-type phase, nm.

	Initial Ga/Mn atomic ratio				Pure reference material from	
	5/1	10/1	20/1	100/1	Ga-precursor, h-GaN	Mn-precursor, c-MnO
			AAVS method			
Derived from aqueous solutions	A5 (57)	A10 (64)	A20 (58)	—	GaN(H_20) (68)	MnO(H_2O)
Derived from methanol solutions	—	B10 (91)	B20 (113)	—	GaN(MeOH) (70)	MnO(MeOH)
			Imide route method			
Pathway 1	—	C10-P1 (15)[a]	—	—	GaN	MnO
Pathway 2	—	C10-P2 (12)[a]	—	C100-P2 (18)[a]	—	—
Pathway 3	—	C10-P3 (33)[a]	—	C100-P3 (28)[a]	—	—

[a] Defected hexagonal phase.

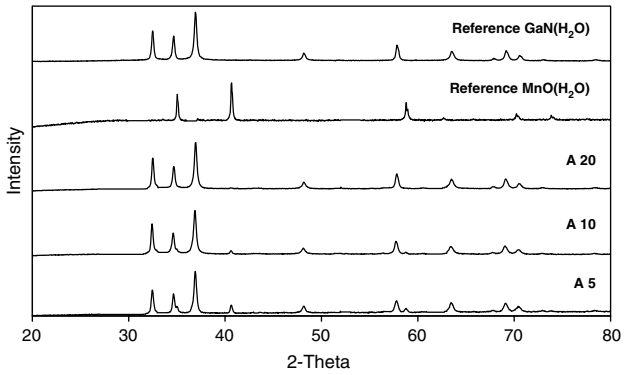

Figure 2. XRD patterns for products and reference samples prepared via the AAVS method from aqueous solutions.

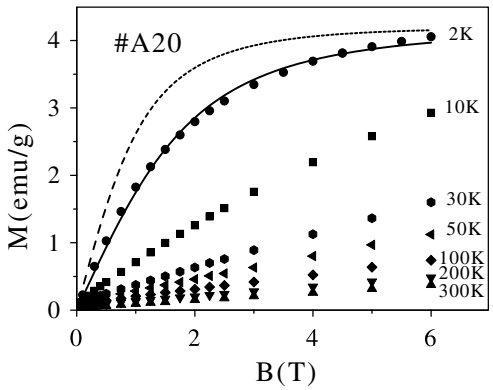

Figure 3. Magnetization of sample A20 (Ga/Mn = 20/1) plotted as a function of magnetic field for several temperatures. The solid and dashed lines represent the effective Brillouin function ($x_{\text{eff}} = 1.24\%$, $T_0 = 1.4$ K) and the standard Brillouin function ($x = 1.25\%$), respectively, calculated for $S = 5/2$ and $T = 2$ K.

For AAVS-derived samples, residual oxygen contents were determined (Saint-Gobain/Carborundum Corp. Boron Nitride, Amherst, NY, USA).

Magnetization of the samples was measured as a function of magnetic field (up to 6 T) and temperature (2–300 K) using a superconducting quantum interference device (SQUID) magnetometer. The powder samples were placed in a glass holder showing controlled diamagnetic signal. In order to reduce the ratio of holder signal to signal of the measured sample, the sample mass was maximized with respect to the upper limit of the SQUID operation range. The magnetization data were corrected in two steps. First, the standard diamagnetic signal of the holder was subtracted from the total signal and, second, the resulting magnetization was further corrected for diamagnetism of pure GaN.

Electron paramagnetic resonance (EPR) measurements were performed using standard X-band spectrometer Bruker ESP-300.

3. Results and discussion

3.1. AAVS method—aqueous solutions

Based on the XRD diffraction patterns shown in figure 2, all three composite powders derived from the different initial Ga/Mn ratios of 5/1, 10/1, and 20/1 (samples A5, A10, and A20, respectively) were composed mostly of the hexagonal GaN-type lattice and accompanying minor cubic MnO. The oxygen analyses and x-ray powder diffraction data revealed increased MnO contents with increasing initial Mn/Ga ratio (or decreasing Ga/Mn ratio). The oxygen content increased from 1.8 to 4.4 wt.% for sample A20 and sample A5, respectively, while being equal to 1.6 wt.% for the 'pure' reference GaN(H_2O) sample due to some residual oxygen from synthesis in the latter. Additionally, the presence of minute quantities of Mn_3N_2 (known to be AF) and Mn_4N (FM up to 700–800 K) in samples A5 and A20 was confirmed from deconvoluted XRD patterns. Based on these characteristics, we expected that a similar magnetic behaviour to that reported for (GaMn)N microcrystals should be observed in our nanocrystalline powders. Indeed, a dominant PM response related to DMS (GaMn)N was observed in all these samples. Minute AF and FM contributions in the total measured magnetization were also observed.

Magnetization measured as a function of the magnetic field up to 6 T at different temperatures for sample A20 (Ga/Mn = 20/1) is depicted in figure 3. In general, the presented data show a typical PM behaviour. At low temperatures (e.g., 2 K), the magnetization reveals a pronounced tendency to saturation with increasing magnetic field while at high temperatures ($T > 50$ K) the magnetization is, practically, a linear function of the magnetic field. The

magnetization saturates with magnetic field (2 K) significantly slower than expected for non-interacting Mn-ions in the d^5 configuration. We recall here that the magnetization of non-interacting magnetic ions should be described by the standard Brillouin function (figure 3). Additionally, a close inspection of the high temperature curves reveals a small linear contribution in the total magnetization most probably originated from MnO. The magnetization of this contribution at 300 K is equal to approximately $M(6\,\mathrm{T}) = 0.2\,\mathrm{emu\,g^{-1}}$.

A dominant PM behaviour very similar to that discussed for sample A20 is also observed in two other samples prepared by the AAVS–aqueous solution method, i.e., samples A5 and A10. However, in the (GaMn)N nanocrystals with the lower initial Ga/Mn ratios of 5/1 and 10/1 (or higher proportions of Mn), due to limited Mn-solubility in GaN, the excess manganese results in increased contents of the MnO by-product in the powders. The highest contribution of MnO is observed in the sample derived from the initial Ga/Mn ratio equal to 5/1. The presence of AF MnO in the sample very clearly manifests itself at high temperatures by an additional linear component in the magnetization versus magnetic field measurements (figure 4(*a*)). The magnetization of sample A5, when measured as a function of temperature at sufficiently low magnetic fields ($B = 0.01$ T and $B = 0.33$ T) to be close to the spontaneous magnetization limit, discloses the presence of AF and FM responses, which accompany the dominant at low temperatures PM response; a well-discernible maximum characteristic for MnO at $T = 118$ K is observed in the curve at $B = 0.33$ T (figure 4(*b*)).

The residual FM response can be extracted (similarly as reported in [28] and [34]) from the magnetization versus magnetic field curves (figure 4(*c*)). The saturation value of magnetization from the determined FM response as above constitutes ca 1.5% of the total magnetization values measured at 2 T and 6 T.

In order to reduce/remove any soluble by-product phases, sample A5 was etched with *aqua regia*. The subsequent magnetization measurements showed a substantial reduction of both the AF response related to MnO (figures 4(*a*) and (*b*)) and FM response (figures 4(*b*) and (*c*)).

Similarly as in the case of sample A5, the magnetization of sample A20 measured as a function of temperature at $B = 0.01$ T and $B = 0.33$ T, besides the PM response, discloses an additional presence of two FM responses, i.e., one with T_C above RT and another with approx. $T_C = 180$ K, respectively. For both contributions, the saturation values of the magnetization inferred from the data ($B = 0.33$ T) are similar and equal to approx. $M_{sat} = 0.04\,\mathrm{emu\,g^{-1}}$. If one assumes that the FM response with T_C above RT originates from Mn_4N (as suggested by XRD data), the amount of the latter should not exceed 0.4% of the sample.

The Mn-concentrations in the DMS (GaMn)N can be estimated from the magnetization data. Regarding the results of EPR experiments (*vide infra*), we describe the experimental data by the Brillouin function with spin $S = 5/2$. However, to take into account the slower saturation effect mentioned above and, therefore, to obtain a reasonable fit the effective temperature of spin system T_{eff} and effective Mn-concentration x_{eff} should be assumed [35], namely,

$$M(B, T) = N \cdot x_{eff} \cdot g \cdot \mu_B \cdot S \cdot B_S(B, T_{eff}), \qquad (1)$$

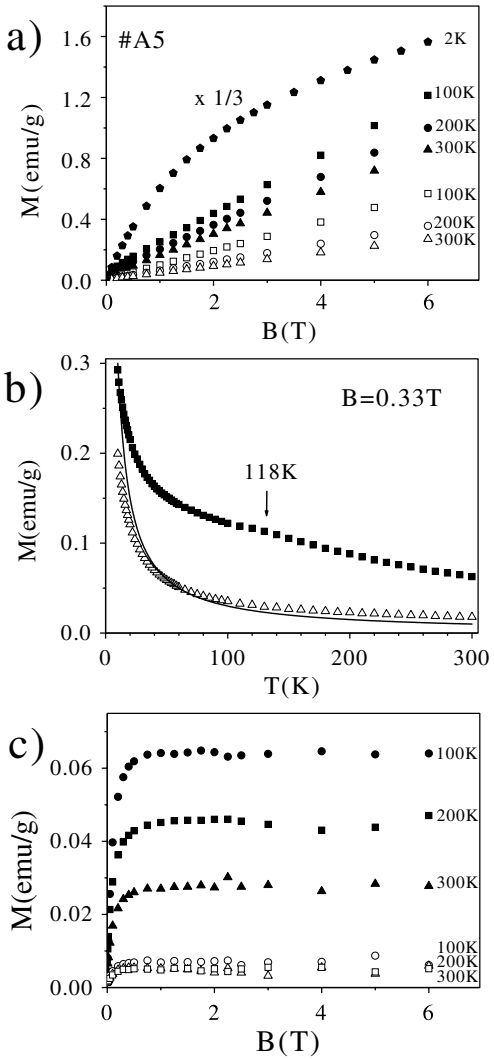

Figure 4. (*a*) Magnetization of sample A5 (Ga/Mn = 5/1) plotted as a function of magnetic field at different temperatures. Measurements performed before and after etching with *aqua regia* are represented by solid and empty marks (squares, circles, triangles), respectively. (*b*) Magnetization of sample A5 (Ga/Mn = 5/1) plotted as a function of temperature for $B = 0.33$ T. Magnetization measurements performed before and after etching with *aqua regia* are represented by solid squares and empty triangles, respectively. The solid line represents the Curie–Weiss law describing the PM phase. (*c*) FM contribution in sample A5 extracted from the total magnetization. Measurements performed before and after etching with *aqua regia* are represented by solid and empty marks (squares, circles, triangles), respectively.

where $T_{eff} = T + T_0$ and x_{eff} are fitting parameters, N is the number of Ga-atoms per mass unit, g is g-factor, and μ_B denotes Bohr magneton. We note that the so-called effective Brillouin function, $B_S(B, T_{eff})$, has been widely and successfully used to describe the magnetization of DMS II–VI compounds doped with Mn [35]. For the AMMONO (GaMn)N microcrystals, the x_{eff} in the range from 0.0022 to 0.061 ($x_{eff} < x$) and relevant T_0 in the range from 0.75 to 2.4 K were reported [8, 9]. We recall that $x_{eff} < x$ and $T_0 > 0$ are both signatures of an AF coupling between magnetic ions [35]. A fit of the effective Brillouin function to magnetization measured as a function of magnetic field at 2 K resulted in

the two fitting parameters. The x_{eff} is nearly the same for all samples and equals to about 1.2% regardless of the initial ratio of Ga/Mn in the precursor system. The values of parameter T_0 approximately equal to 1.4 K indicate an AF interaction between Mn-ions. Thus, the presented results are in general accord with those reported earlier for the AMMONO (GaMn)N microcrystals [8, 9].

The reference sample $MnO(H_2O)$ obtained from processing of pure manganese (II) nitrate solution shows an AF response with Néel temperature, T_N, of approx. 118 K characteristic for MnO which is corroborated by the results of x-ray powder diffraction and O-analysis. The reference sample $GaN(H_20)$ made from processing of pure gallium nitrate solution reveals a weak PM response with a magnetization value about 14 times smaller than those for samples intentionally doped with Mn. Additionally, a very weak FM response with T_C above RT is derived for this sample from temperature dependent magnetization measurements performed at low magnetic field ($B = 0.01$ T).

The EPR measurements reveal for each sample (A5, A10, A20) a single, structureless resonance line with a g-factor equal to 2.008 ± 0.003 and the peak-to-peak line width equal to about 32 mT (for more details, see [32]). In this regard, the Mn^{+2}-ions ($3d^5$, $S = 5/2$, $I = 5/2$) were observed in the EPR studies of thin GaN layers grown on the 6H–SiC substrate by the 'sandwich method' [36]. Therein, the line of $g = 1.999$ showed a fine splitting into five components each with a sixfold hyperfine splitting due to the interaction of an electron with a Mn-nuclear spin. In the previously mentioned studies [8, 9], the EPR experiments were performed on the $Ga_{1-x}Mn_xN$ microcrystals grown by the AMMONO method with Mn-concentrations x ranging from 0.000 05 to 0.096. For all these samples, a single EPR line with a g-factor equal to 1.999 was observed. However, a six-line hyperfine structure was only visible for samples with the lower Mn-contents ($x \leqslant 0.001$) while a single broad line was found in all samples with the higher Mn-contents. The line seen in the EPR experiments was ascribed to $Mn^{+2}(d^5)$-centres and related to the central group of lines reported in [36] ($M_s = 1/2 \longleftrightarrow M_s = -1/2$). Similarly, only the central group of lines has been observed in the amorphous ZnO : Mn [37] and ZnS : Mn [38] powders. In the latter case, a slightly higher g-factor for the interacting versus isolated Mn-ions was reported. The broadening of the hyperfine line structure with increasing Mn-concentrations is well known for II–VI Mn-based DMS and has been observed in (GaMn)As as well [39]. The presence of the characteristic single, broad line in different highly Mn-doped semiconductors was ascribed to Mn^{+2}-pairs or larger clusters of interacting Mn-ions [40, 41].

The shape and width of the EPR line observed in the (GaMn)N nanocrystals derived from aqueous solutions indicate an exchange interaction between Mn^{2+}-ions. Thus, the presence of the AF interaction between Mn-ions suggested by the magnetization data is in accord with the EPR results. Our magnetization and EPR experiments provide strong arguments that the magnetic properties of the (GaMn)N nanocrystalline powders prepared by the AAVS method via aqueous solutions are similar to those of the (GaMn)N microcrystals obtained by the AMMONO method [8, 9].

3.2. AAVS method—methanol-based solutions

The XRD patterns (not shown) and oxygen analyses imply that the nanocrystalline powders obtained with the AAVS method from methanol-based solutions are in terms of composition, roughly, similar to those derived from the aqueous solutions discussed above, i.e., they are by XRD spectroscopy composed of the prevailing hexagonal GaN-type lattice and minor cubic phase of MnO. The O-contents for the products from system Ga/Mn = 20/1 (sample B20) and Ga/Mn = 10/1 (sample B10) are equal to 0.9 wt.% and 1.9 wt.%, respectively, and for the reference samples of GaN(MeOH) and MnO(MeOH), 1.0 wt.% and 23.2 wt.% (theor. O-content in MnO, 22.6 wt.%), respectively. As expected, based on the advantageous effect of carbothermal reduction/nitridation associated with the use of methanol, the O-contents appear to be lower in the powders derived from the methanol-based solutions than in the comparable powders derived from the aqueous solutions.

Magnetization measured for the powders as a function of magnetic field reveals a typical PM behaviour very similar to that observed for the (GaMn)N powders derived from the aqueous solutions. Detailed data analysis shows that in samples B10 and B20 the Mn-content reaches approx. 1.1% (*vide infra*, magnetization curve for sample B20 in figure 8), thus being only slightly smaller than in the comparable materials from aqueous solutions (samples A5, A10, and A20). Also, similarly as in the case of the latter materials, an increase in the initial Mn-content when going from sample B20 to sample B10 causes an increase in the MnO-component contribution in total magnetization (linear contribution discernible at high temperatures in the magnetization versus magnetic field curves). Additionally, the temperature dependent magnetization measurements performed at two magnetic fields ($B = 0.01$ T and $B = 0.33$ T) reveal residual by-product phases or precipitates in samples B10 and B20 (quantities one order of magnitude smaller than those in the relevant samples A5, A10, and A20). Also, a minute FM response with T_C below room temperature, visible as a discernible shoulder on the magnetization versus temperature curve, was detected in sample B10.

The reference sample MnO(MeOH) synthesized from the pure manganese precursor shows the AF response with Néel temperature, T_N, of approx. 118 K, which is characteristic for MnO. The exclusive presence of the latter is also supported by the XRD pattern and O-analysis for the sample. The reference sample GaN(MeOH) (pure, not intentionally doped GaN) reveals a very weak FM response of approx. $M_{\text{sat}} = 0.6\ \text{emu g}^{-1}$ with T_C above room temperature.

The EPR measurements for both samples B10 and B20 show a single, broad resonance line with a g-factor equal to 2.008 ± 0.003 and the peak-to-peak line width equal to about 32 mT (for details, see [32]). These values are comparable with the relevant quantities in the aqueous system and support a similar nature of the Mn-dopant, i.e., the presence of $Mn^{+2}(d^5)$-centres in both systems.

3.3. Imide route method

In order to obtain (GaMn)N powders with potentially even lower residual O-contents and smaller crystallite sizes in the nanosized range, we adopted the anaerobic imide route

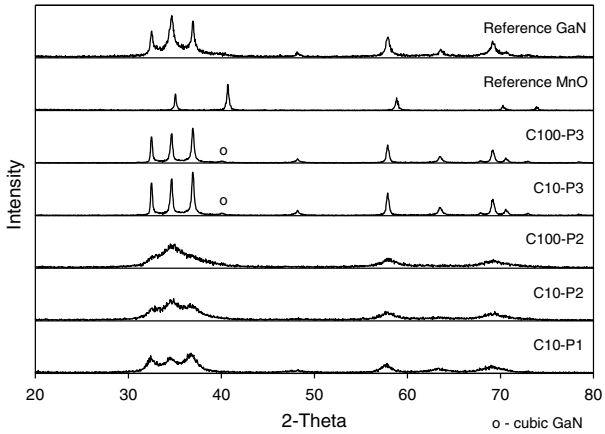

Figure 5. XRD patterns for products and reference samples prepared via anaerobic imide route method.

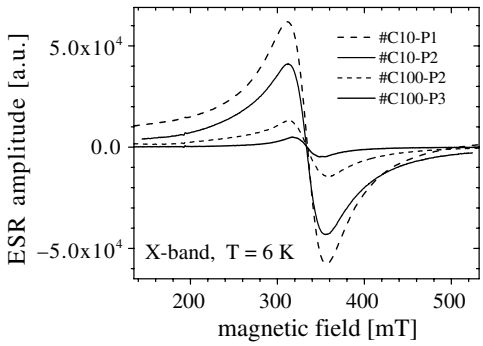

Figure 6. Normalized EPR resonance lines of nanocrystalline powders obtained via imide route.

previously successfully used to make powders of pure GaN [33]. We also chose to introduce the Mn-dopant to GaN at different stages of the reaction scheme to yield samples C10-P1, C10-P2, C100-P2, C10-P3, and C100-P3 as described in the experimental.

The XRD diffraction patterns of samples C10-P1, C10-P2, C100-P2, C10-P3, and C100-P3 are included in figure 5. They display a range of mostly defected hexagonal GaN-lattices typical for GaN prepared via imide route [33] and other anaerobic preparation methods [42]. In particular, the least defected hexagonal phase of nanocrystalline (GaMn)N is observed in the case of sample C10-P1 from Pathway 1. On the other hand, heavily defected hexagonal nanostructures of (GaMn)N are inferred in samples C10-P2 and C100-P2 originating from Pathway 2. Finally, strong and relatively narrow peaks characteristic for the hexagonal phase are accompanied by very weak peaks assigned to cubic GaN in the diffraction patterns of samples C10-P3 and C100-P3 from Pathway 3. In the diffraction pattern of sample C10-P3, weak peaks for the cubic MnO by-product are also discernible.

The representative EPR data for materials obtained via imide route are shown in figure 6. Generally, all EPR spectra of (GaMn)N nanocrystals reveal a single, broad, and structureless resonance line with a g-factor equal to 2.008 ± 0.003. The peak-to-peak EPR line widths are similar for the samples from Pathway 1 (sample C10-P1) and Pathway 2 (sample C10-P2 and sample C100-P2) that show, relatively, higher Mn-contents and smaller average crystallite sizes, i.e., C10-P1, 44.6 mT; C10-P2, 44 mT; C100-P2, 45.5 mT while for the samples from

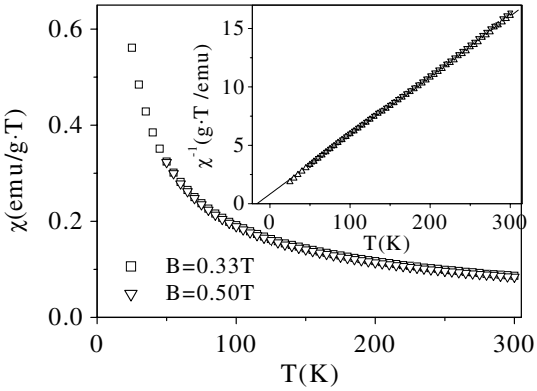

Figure 7. Susceptibility ($\chi = M/B$) of sample C10-P1 plotted as a function of temperature for $B = 0.33$ T and $B = 0.5$ T. Inset shows the plot of inverse susceptibility versus temperature (corrected for temperature independent contribution M_0).

Pathway 3 with the lower Mn-contents and larger average crystallite sizes the EPR line width is smaller, i.e., C100-P3, 38 mT (see also table 1). We recall that the resonance lines of samples prepared by the AAVS method showed the same g-factor while their line widths were equal to 32 mT. The shape and widths of the EPR lines observed in the (GaMn)N nanocrystals obtained by this method indicate an exchange interaction between Mn^{2+} ions which is further corroborated by the magnetization data discussed below.

It appears that the Mn-concentration in the (GaMn)N nanocrystals obtained via imide route is strongly dependent on the stage of Mn-introduction into the reaction system. In this regard, the highest Mn-content was found in sample C10-P1 in which the manganese precursor was added at the earliest stage of synthesis. In general, magnetization as a function of magnetic field for sample C10-P1, at different temperatures, is similar in form to that of sample A20 (figure 3) but higher in magnitude by a factor of 2. Additionally, a close inspection of the magnetization versus magnetic field curve measured at 2 K reveals a less pronounced saturation with increasing magnetic field for sample C10-P1 than that observed in the relevant case of sample A20. The effective Brillouin function fit of the magnetization curve ($T = 2$ K) returned x_{eff} and T_{o} equal to approx. 2.9% and 2 K, respectively. This T_0 value, higher than the T_0 value extracted for sample A20, suggests a much stronger AF interaction between Mn-ions in sample C10-P1 than in sample A20. To investigate further the magnetic behaviour of sample C10-P1, the magnetization was measured as a function of temperature at three different magnetic field levels ($B = 0.01$ T, 0.33 T, and 0.5 T), i.e., in the linear response range.

In general, a Curie–Weiss (C–W)-like contribution ($\chi \propto 1/T$) dominates the data (figure 7). However, analysis of the magnetization from the high temperature range reveals the presence of a small background contribution in the total magnetization, which is most probably related to some FM/MnO precipitates or other residual by-products. In order to quantitatively analyse the magnetization data, we use a rough assumption about the background, i.e., temperature independent contribution, $M_0 = \text{const}$. The magnetization of sample C10-P1 is corrected for M_0 (extracted from the $M(T) \cdot T$ versus T plot in the high temperature range) and, then, the inverse susceptibility ($\chi = M/B$) versus temperature is plotted (see inset in figure 7). It follows that the experimental points are well described by a

linear function intersecting the temperature axis at temperature $T = \Theta$ (Curie–Weiss temperature) equal to -16 ± 3 K.

The data were also analysed in the following independent way. A simple three-parameter formula was fitted to the measured susceptibility

$$\chi(T) = C/(T - \Theta) + \chi_0, \tag{2}$$

where χ_0 represents temperature-independent contribution while PM contribution attributed to manganese ions from the (GaMn)N nanocrystals is described by the Curie–Weiss law. The derived temperature $\Theta = -14 \pm 5$ K for sample C10-P1 from the fit of equation (2) to χ_{exp} versus T curves ($B_0 = 0.33$ T and $B_0 = 0.5$ T) is consistent with the Θ-value obtained from the inverse susceptibility versus temperature plot as described above. The Mn-concentration x can be estimated from the C–W constant C which, for a given value of x, can be calculated in the following way:

$$C = N \cdot x \cdot (g \cdot \mu_B)^2 \cdot S \cdot (S + 1)/3k_B, \tag{3}$$

where N is the number of Ga-atoms per mass unit, k_B is Boltzmann constant, and S denotes spin of Mn-ion. Regarding the results of EPR, i.e., assuming manganese ions in the $Mn^{2+}(d^5)$-configuration ($S = 5/2$), the concentration x can be calculated from equation (3). Thus, the estimated x value equal to $3.5 \pm 0.3\%$ is consistent with the value obtained earlier from the fit of the effective Brillouin function to the magnetization versus magnetic field curve measured at 2 K. We recall, that $x_{eff} < x$ reflects the AF interaction between Mn-ions.

Similarly to sample C10-P1 from Pathway 1, both Pathway 2 products, i.e., samples C10-P2 and C100-P2, also show an overall PM behaviour well described by the effective Brillouin function with $S = 5/2$ but with lower x_{eff}. Comparison of the Mn-concentrations in the (GaMn)N nanocrystals from different samples can be readily performed based on the magnetization curves collected in figure 8. Generally, at low temperatures the magnetization of the PM phase saturates, relatively, at a low magnetic field. The M_{sat} value, in turn, is proportional to the Mn-concentration in the (GaMn)N nanocrystals. Since in terms of our experiment $M(6\,T, 2\,K)$ is roughly equal to M_{sat}, therefore the $M(6\,T, 2\,K)$ values equal to 9.3, 6.7, and 2.8 emu g^{-1} for samples C10-P1, C10-P2, and C100-P2, respectively, indicate the smallest Mn-concentration x in sample C100-P2 (figure 8). The latter concentration is more than three and two times lower than x in samples C10-P1 and C10-P2, respectively.

According to the XRD and magnetization studies, in the case of the surface-modified GaN materials from Pathway 3, e.g., samples C10-P3 and C100-P3, our goal was only partially attained. We recall that the major thrust of the study was to obtain phase-homogeneous (GaMn)N nanocrystalline powders with the highest possible Mn-contents. Firstly, the XRD pattern of sample C10-P3 reveals that the prevailing hexagonal GaN-type phase is accompanied by the minor cubic MnO phase. This observation is corroborated by the magnetization data which reveal the presence of comparable PM and AF contributions. The magnetization measured as a function of magnetic field shows that the total magnetization is a sum of the linear contribution, dominant at high temperatures and related to MnO, and the PM contribution distinct by

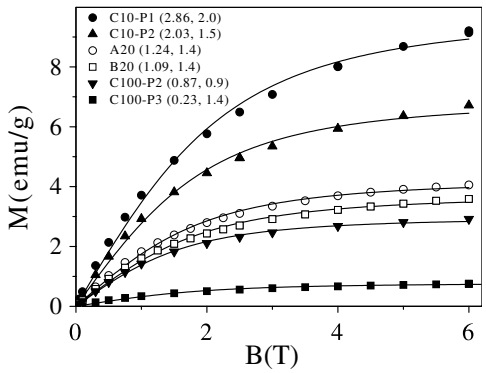

Figure 8. Comparison of magnetization plotted as a function of magnetic field measured at $T = 2$ K for different samples. The solid lines represent fits of the effective Brillouin function to experimental points. Empty circles and squares are for samples prepared via AAVS while solid circles, triangles and squares are for samples prepared via the imide route. In the legend are included the labels of samples and x_{eff} and T_0 values (in parentheses).

the characteristic saturation with increasing magnetic field at low temperatures (2 K curve) that is related to (GaMn)N. The C–W-like ($\chi \propto 1/T$) response superimposed on the AF response with the characteristic for MnO well-discernible maximum at $T = 118$ K are observed in the temperature dependent magnetization curves. Secondly, by subtracting the AF contribution from the total magnetization (M versus B curve, $T = 2$ K) we could estimate the PM contributions and Mn-concentrations in the host (GaMn)N nanocrystals. The value of approx. $M(6\,T, 2\,K) = 1$ emu g^{-1} indicates that the Mn-concentration in (GaMn)N obtained via Pathway 3 (sample C10-P3) is about 0.2%, thus being much smaller than that in sample C10-P1. Increasing the initial Ga/Mn ratio from 10/1 (sample C10-P3) to 100/1 (sample C100-P3) gives rise to the substantial reduction of the MnO by-product in the system (considerable decrease of the linear contribution in the magnetization versus magnetic field curve, $T = 300$ K) while the Mn-concentration in the (GaMn)N nanocrystals is not substantially lowered (approx. $M(6\,T, 2\,K) = 0.8$ emu g^{-1}).

4. Conclusions

In conclusion, we demonstrate that the (GaMn)N nanocrystalline powders with relatively high Mn-contents can be successfully prepared by two different methods, i.e., AAVS and the imide route. The Mn-concentrations of the AASV samples, estimated from the magnetization data, are nearly the same (about 1.1–1.2%) for all the samples regardless of both the initial ratio of Ga/Mn (different proportions of the manganese precursor) and the kind of solvent used in the process. The Mn-concentrations in the (GaMn)N nanocrystalline powders obtained via the imide route prove to be strongly dependent on the stage of Mn-introduction into the system. The maximum observed Mn-concentration amounts to about 3.5%, thus being approx. thrice as high as in the AAVS-derived samples.

All investigated samples show a dominant PM behaviour well described by the Brillouin function with $S = 5/2$. Small AF and FM contributions are also observed and they are much lower in the (GaMn)N nanocrystals obtained by the imide route than in those obtained by the AAVS method. The main

contribution to the AF response results from the MnO by-product.

The observed slower magnetization saturation with magnetic field than predicted by the standard Brillouin function valid for non-interacting ions, more pronounced for the samples with high Mn-concentrations, reflects the AF-interaction between Mn-ions. The measured temperature dependence of magnetic susceptibility is well described by the Curie–Weiss law with negative Curie–Weiss temperature. This negative temperature clearly indicates an AF coupling between Mn-ions corroborating the conclusion derived from the low temperature magnetization study. The interaction between Mn-ions is further confirmed by the EPR study. The recorded in all samples single, structureless resonance line with a g-factor equal to 2.008 ± 0.003 suggests the presence of $Mn^{2+}(d^5)$-centres. The shape of the line and its width indicate an exchange interaction between Mn-ions. The observed line broadening is accompanied by increasing Mn-contents and decreasing average crystallite sizes, the latter coinciding with deterioration of the hexagonal structure of (GaMn)N.

The magnetization and EPR data show very similar general properties of the (GaMn)N nanocrystalline powders prepared by the AAVS and imide route methods with the (GaMn)N microcrystals obtained previously by the AMMONO method [8, 9]. The AF interactions between Mn-ions, inferred from the negative C–W temperature Θ, were also observed in the (GaMn)N thin layers [26]. It is worth noting that ferromagnetism previously observed at RT and above for the (GaMn)N microcrystals [28] and (GaMn)N layers [26] was shown not to be an intrinsic property of homogeneous (GaMn)N lattices but rather originating from precipitates or nanometre-scale Mn-rich clusters formed during crystal growth. In our (GaMn)N nanocrystalline powders, in addition to minute quantities of FM precipitates/clusters, the undesirable MnO by-product is also present. In our opinion, substantial reduction/elimination of MnO in the powders can likely be achieved by further refinement of the synthetic methods.

Acknowledgments

Support from the Ministry of Education and Science (Poland) is acknowledged, in particular under Grant 3 T08D 042 26. R T Paine wants to acknowledge the support of the US National Science Foundation, Grant CHE-9983205.

References

[1] Ohno H 1998 *Science* **281** 951
[2] Ohno H, Munekata H, Penney T, Von Molnar S and Chang L L 1992 *Phys Rev. Lett.* **68** 2664
[3] Liu C, Yun F and Morkoc H 2005 *J. Mater. Sci. Mater. Electron.* **16** 555
[4] Dietl T, Ohno H, Matsukara F, Cibert J and Ferrand D 2000 *Science* **287** 1019
[5] Graf T, Gjukic M, Brandt M S, Stutzmann M and Ambacher O 2002 *Appl. Phys. Lett.* **81** 5159
[6] Graf T, Gjukic M, Herman M, Brandt M S, Stutzmann M and Ambacher O 2003 *Phys. Rev.* B **67** 165215
[7] Wołoś A, Palczewska M, Zając M, Gosk J, Kamińska M, Twardowski A, Boćkowski M, Grzegory I and Porowski S 2004 *Phys. Rev.* B **69** 115210
[8] Zając M, Doradziński R, Gosk J, Szczytko J, Lefeld-Sosnowska M, Kamińska M, Twardowski A, Palczewska M, Grzanka E and Gębicki W 2001 *Appl. Phys. Lett.* **78** 1276
[9] Zając M, Gosk J, Kamińska M, Twardowski A, Szyszko T and Podsiadło S 2001 *Appl. Phys. Lett.* **79** 2432
[10] Szyszko T, Kamler G, Strojek B, Weisbrod G, Podsiadło S, Adamowicz A, Gębicki W, Szczytko J, Twardowski A and Sikorski K 2001 *J. Cryst. Growth* **233** 631
[11] Kuwabara S, Ishii K, Haneda S, Kondo T and Munekata H 2001 *Physica* E **10** 233
[12] Sasaki T, Sonoda S, Yamamoto Y, Suga K, Shimizu S, Kindo K and Hori H 2002 *J. Appl. Phys.* **91** 7911
[13] Theodoropoulou N, Hebard A F, Overberg M E, Abernathy C R, Pearton S J, Chu S N G and Wilson G 2001 *Appl. Phys. Lett.* **78** 3475
[14] Reed M L, El-Masry N A, Stadelmaier M H, Ritums H K, Reed M J, Parker C A, Roberts J C and Bedair S 2001 *Appl. Phys. Lett.* **79** 3473
[15] Sato K and Katayama-Yoshida H 2001 *Japan. J. Appl. Phys.* 2 **40** L485
[16] Katayama-Yoshida H, Kato R and Yamamoto T 2001 *J. Cryst. Growth* **231** 428
[17] Van Schilfgaarde M and Mryasov O N 2001 *Phys. Rev.* B **63** 233205
[18] Kulatov E, Nakayama H, Mariette H, Ohta H and Uspenskii Yu A 2002 *Phys. Rev.* B **63** 045203
[19] Kronik L, Jain M and Chelikowsky J R 2002 *Phys. Rev.* B **66** 041203(R)
[20] Mahadevan P and Zunger A 2004 *Appl. Phys. Lett.* **85** 2860
Mahadevan P and Zunger A 2004 *Phys. Rev.* B **69** 115211
[21] Bogusławski P and Bernholc J 2005 *Phys. Rev.* B **72** 115208
[22] Dhar S, Brandt O, Trampert A, Däweritz L, Friedland K J, Ploog K H, Keller J, Beschoten B and Güntherodt G 2003 *Appl. Phys. Lett.* **82** 2077
[23] Chen P P, Makino H, Kim J J and Yao T 2003 *J. Cryst. Growth* **251** 331
[24] Shon Y, Kwon Y H, Yuldashev Sh U, Leem J H, Park C S, Fu D J, Kim H J, Kang T W and Fan X J 2002 *Appl. Phys. Lett.* **81** 1845
[25] Kuwabara S, Kondo T, Chikyow T, Ahmet P and Munekata H 2001 *Japan. J. Appl. Phys.* 2 **40** L74
[26] Dhar S, Brandt O, Trampert A, Friedland K J, Sun Y J and Ploog K H 2003 *Phys. Rev.* B **67** 165205
[27] Cui Y and Li L 2002 *Appl. Phys. Lett.* **80** 4139
[28] Zając M, Gosk J, Grzanka E, Kamińska M, Twardowski A, Strojek B, Szyszko T and Podsiadło S 2003 *J. Appl. Phys.* **93** 4715
[29] Ando K, Saito H I, Zayets V and Debath M C 2004 *J. Phys.: Condens. Matter.* **16** S5541
[30] Ando K 2003 *Appl. Phys. Lett.* **82** 100
[31] Ploog K H, Dhar S and Trampert A 2003 *J. Vac. Sci. Technol.* B **21** 1756
[32] Janik J F, Drygaś M, Czosnek C, Kamińska M, Palczewska M and Paine R T 2004 *J. Phys. Chem. Solids* **65** 639
[33] Janik J F and Wells R L 1996 *Chem. Mater.* **8** 2708
[34] Gosk J, Zajac M, Byszewski M, Szczytko J, Twardowski A, Strojek B and Podsiadło S 2003 *J. Supercond.* **16** 79
[35] Gaj J A, Planel R and Fishman G 1979 *Solid State Commun.* **29** 435
[36] Baranov P G 1996 *Semicond. Sci. Technol.* **11** 1843
[37] Volkel G, Poppl A and Voigtsbeerger B 1988 *Phys. Stat. Solidi* a **109** 295
[38] Kreissl J 1986 *Phys. Stat. Solidi* a **97** 191
[39] Szczytko J, Twardowski A, Świątek K, Palczewska M, Tanaka M, Hayashi T and Ando K 1999 *Phys. Rev.* B **60** 8304
[40] Ishikawa Y 1966 *J. Phys. Soc. Japan* **21** 1473
[41] Lu X, Chen C, Husurianto S and Koretsky M D 1999 *J. Appl. Phys.* **85** 4154
[42] Hwang J W, Campbell J P, Kozubowski J, Hanson S A, Evans J F and Gladfelter W L 1995 *Chem. Mater.* **7** 517